

<https://doi.org/10.1038/s41529-024-00443-z>

Electrodeposited graphene/layered double hydroxides micro/nanocontainers for both passive and active corrosion protection

Teng Xu¹, Qian-Yu Wang¹, Jin-Tao Zhang² & Ji-Ming Hu¹ ✉

The poor dispersibility of layered double hydroxides (LDHs) is considered to be the main drawback limiting their application in anti-corrosive coatings. In this work, the problem is solved by combining LDHs with graphene (Gr). A facile electrochemically assisted deposition technique (EAT) is developed to prepare Gr/LDH micro/nano-containers. The high-barrier Gr and LDHs synergistically build a 'labyrinth effect' to lengthen the diffusion path of corrosive mediums. Moreover, corrosion inhibitors can be released from the interlayer galleries of LDHs and impede corrosion of metal substrate by substituting the aggressive ions. Therefore, the polyvinyl butyral (PVB) coatings doped with Gr/LDH micro/nano-containers pre-loaded with inhibitors 2-Mercaptobenzothiazole (MBT) have both passive and active corrosion protection properties and provide excellent protection to copper substrate.

Metal corrosion has been, and continues to be the focus of scientific research due to potential security risks and enormous economic losses^{1,2}. Polymer coatings are one of the most effective and widespread solutions to the problems caused by the corrosion of metals^{3,4}. As barrier layers, polymer coatings can prevent direct contact between metal substrates and aggressive medium. However, due to the volatilization of solvent, shrinkages and internal defects inevitably occur in polymer coatings during the curing process. As a result, traditional coatings do not provide sufficient long-lasting protection for metal substrates because their structural defects cause fast diffusion of corrosion medium into the coating matrix and subsequently lead to coating failure and metal corrosion⁵⁻⁷. Therefore, there is an urgent need to improve the anti-corrosion properties of traditional polymer coatings.

In recent years, polymer coatings that provide both passive and active protection have received widespread attention. Passive protection focuses on delaying the penetration of corrosive ions into the coating matrix⁸⁻¹⁰. Active corrosion protection aims to reduce the corrosion rate when the polymer coating is damaged, and corrosive ions diffuse into the coating/metal interface¹¹⁻¹³. Passive protection can be achieved by adding two-dimensional materials into polymer coatings, and active protection is provided by incorporating corrosion inhibitors^{14,15}. However, the directly incorporated inhibitors may damage the entirety of the coating system and tend to leak from the coating matrix during service^{16,17}. One way to avoid the above

drawback is to encapsulate corrosion inhibitors in nanocontainers and then incorporate the inhibitor-loaded nanocontainers into the coating matrix¹⁸⁻²⁰. Nanocontainers are a type of nanomaterials possessing large specific surface area and stimuli-responsive properties. They can actively perceive the changes in the local environment, such as ionic strength^{21,22}, local pH^{23,24}, humidity^{25,26}, light^{27,28}, and so on, and then release encapsulated corrosion inhibitors to target sites, which meet the demand of active protection.

A number of nanocontainers have been developed, such as mesoporous SiO₂^{29,30}, halloysite nanotubes^{31,32}, layered double hydroxides (LDHs)^{33,34}, metal-organic frameworks (MOFs)^{35,36}, and so on. Among these nanomaterials, LDHs nanocontainers not only possess the ability to store and release corrosion inhibitors but also exhibit typical two-dimensional lamellar structure, which ensures LDHs-based polymer coatings have both active and passive protecting capabilities³⁷⁻³⁹. However, due to the structural characteristics of LDHs nanoflakes themselves, they are prone to severe agglomeration when incorporated into the coating resin⁴⁰. The heavy aggregation of LDH nanoflakes leads to their non-uniform dispersion in coatings, which is the main drawback of their application in polymer coatings⁴¹.

Tailoring LDHs structure with other materials is a promising way to achieve more uniform dispersion in the coating matrix. In fact, some LDHs-based composites, such as graphene oxide (GO)/LDH^{42,43}, Mxene/LDH^{44,45}, MoS₂/LDH⁴⁶, have been developed, and the polymeric coatings doped with

¹Department of Chemistry, Zhejiang University, Hangzhou 310027, P.R. China. ²College of Chemical engineering and Materials, Changzhou Institute of Technology, Changzhou 213032, China. ✉e-mail: kejmh@zju.edu.cn

these nanocontainers possess both passive and active protecting capabilities. However, the substrates of the above composite nanocontainers are mainly limited to costly GO and Mxene. Moreover, the industrial scale preparation of GO or Mxene is generally carried out under harsh conditions, including the massive use of environmentally hazardous reagents⁴⁷. Additionally, solvothermal synthesis is the common method for preparing these LDH-based composite nanocontainers, which is time-consuming and energy-intensive⁴⁸. Therefore, it is crucial to develop a simple and low-energy method to prepare low-cost LDH-based composite nanocontainers.

Recently, our group developed an electrochemically assisted sol-gel deposition technique (EAT) to fabricate graphene/silica (Gr/SiO₂) nanocomposites^{49,50}. EAT commonly utilizes the OH⁻ (or H⁺) generated by the reaction on the electrode to catalyze the condensation polymerization of the precursor into a film. In this work, based on the dominant role of OH⁻ in the nucleation and growth of LDHs nanoflakes, EAT is employed to fabricate Gr/LDH composite. The sandwich-like Gr/LDH composites were successfully prepared by EAT and further used as micro/nano-containers for loading corrosion inhibitors (based on the particle size of Gr/LDH composite, it is more appropriate to name the composite micro/nano-container, which will be explained in detail in the following text). EAT technology makes the deposited LDH nanoflakes uniformly dispersed on the surface of graphene, which overcomes the shortcomings of traditional LDH nanocontainers that lack satisfactory barrier properties due to their agglomerations. Thus, in these micro/nano-containers, Gr and LDH synergistically provide passive barrier functions, and meanwhile, the LDH nanoflakes function as corrosion inhibitor containers to ensure active protective properties. Gr/LDH micro/nano-containers were pre-loaded with 2-Mercaptobenzothiazole (MBT), a type of green corrosion inhibitor for copper, and then added into the matrix of polyvinyl butyral (PVB) resins. Experimental results show that the PVB coatings doped with (Gr/LDH)@MBT exhibit excellent protective properties against corrosion.

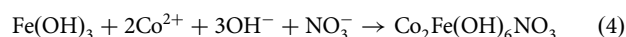
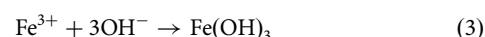
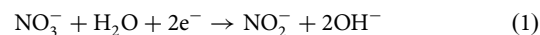
Notably, the advantages of using Gr are that, apart from eliminating the use of hazardous and polluting chemicals for GO preparation, Gr has better barrier and mechanical properties than GO due to the expansion of C-C bond length during graphene oxidation^{51,52}. In addition, the highly conjugated structure of Gr is more conductive than GO, which fulfills the essential requirement of EAT.

Results

Characterization of micro/nano-containers

The electrodeposition process was conducted in a three-electrode cell. A platinum-net electrode, an Ag/AgCl (saturated KCl) electrode, and a

platinum foil electrode (40 cm²) were used as counter, reference, and working electrode, respectively. A schematic diagram of the electrochemically assisted preparation of Gr/LDH nanocomposite is depicted in Fig. 1. Ideally, when an appropriate cathodic potential is applied, water and nitrate ions (NO₃⁻) will be reduced to generate hydroxide ions (OH⁻) on the surface of Gr (Eqs. (1) and (2)). Subsequently, the generated OH⁻ ions first react with Fe³⁺ ions to form Fe(OH)₃ (Eq. 3), because Fe(OH)₃ has a smaller K_{sp} value (Fe(OH)₃: 4 × 10⁻³⁸, Co(OH)₂: 2 × 10⁻¹⁵)^{53,54}. As the reduction reaction proceeds, the concentration of OH⁻ on the Gr surface becomes higher. The OH⁻ ions react with Co²⁺ and finally cover into CoFe-LDH with NO₃⁻ intercalation (Eq. 4)⁵⁵.



The current density–time curve during electrochemically assisted preparation of Gr/LDH at different potentials is shown in Supplementary Fig. 1. In the early stages of electro-assisted deposition, the current density decreases rapidly and then keeps on a steady value. The negative shift of deposition potential promotes the formation of OH⁻ ions and thus accelerates the growth of LDH. Supplementary Figs. 2 and 3 show a series of SEM images obtained at different deposition potentials and deposition times, respectively. It can be seen that LDH nanoflakes tended to grow gradually on the surface of Gr with the negative shift of the deposition potential and the prolonging of the deposition time. Considering the coverage and the dispersion of the deposited LDH nanoflakes on the Gr surface, ‘-1.1 V, 40 min’ was chosen as the optimal deposition condition.

The SEM and TEM images of different samples are shown in Fig. 2. Pure graphene presents a two-dimensional (2D) sheet-like structure with many wrinkles (Fig. 2a, a₁). After the electrodeposition of LDHs, both sides of graphene are almost completely covered by LDHs nanoflakes (Fig. 2b, b₁), resulting in a sandwich-like structure. Notably, the as-deposited LDHs nanoflakes are uniformly and vertically dispersed on both sides of graphene due to electrostatic repulsions and bridging of hydrogen bonds among LDHs. It is worth noting that EAT provides excellent adhesion between Gr

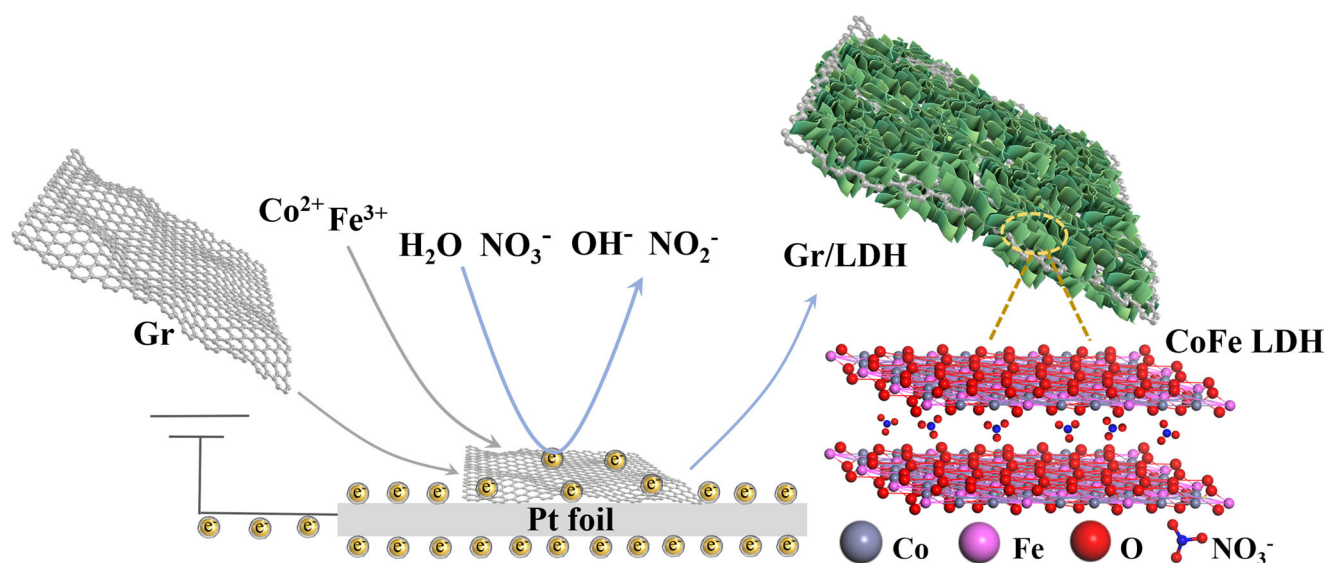


Fig. 1 | Electrochemical deposition composite. Schematic illustration of electrochemically assisted deposition of LDH nanoflakes on graphene nanosheets.

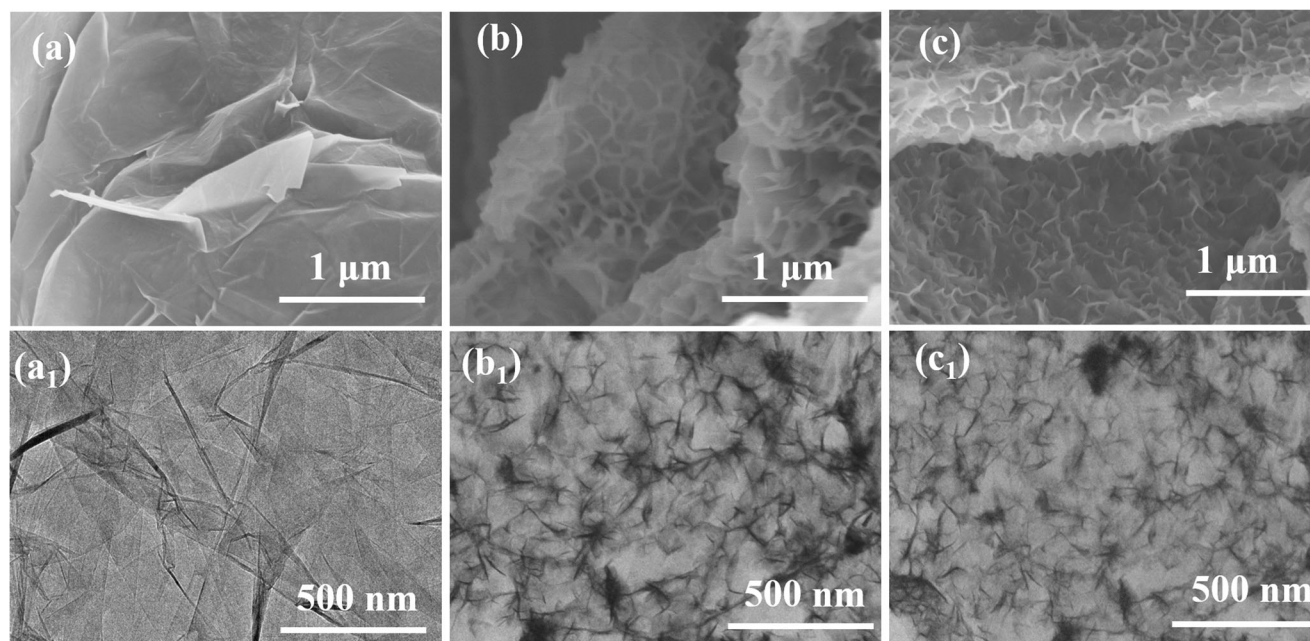


Fig. 2 | Morphology of different samples. a–c SEM and a₁–c₁ TEM images of a, a₁ Gr, b, b₁ Gr/LDH obtained under optimization condition and c, c₁ Gr/LDH after ultrasonic oscillation for 2 h.

nanosheets and LDHs nanoplates so that the deposited LDHs nanoplates are still firmly attached to the upper and lower surface of graphene even after ultrasonic treatment for 2 h (Fig. 2c, c₁).

The HRTEM and corresponding element mapping images (Fig. 3a, b) reveal homogeneous dispersions of C, O, Co, and Fe over the whole surface of graphene, proving that the deposited LDHs nanoplates are evenly distributed on the graphene surface. As shown in Fig. 3, the thickness of the bare graphene nanosheet is around 1.8 nm. Benefiting from the significant driving force for the growth of LDHs nanoflakes provided by the electrochemically assisted deposition technique (EAT), Gr/LDH composite nanosheets reach a thickness of up to 70 nm within half an hour. As described in SEM (Fig. 2) and AFM (Fig. 3c, d), graphene sheets have an average 2D diameter of ~2 μm, and LDH sheets have a thickness of ~70 nm. The Gr/LDH composites have both micro and nano characteristics. Therefore, it is more accurate to name the Gr/LDH composite as a micro/nano-container.

The results of XRD also confirm that the major crystalline component on Gr surface is the deposited LDH, as shown in Fig. 4a. The peaks corresponding to the (003) (10.18°), (006) (20.86°), and (012) (34.24°) diffractions of Gr/LDH are attributed to the characteristic diffraction of typical hydroxide-like structure, which is consistent with previous reports⁵⁶. The (003) basal spacing (d_{003}) of the deposited LDH is determined to be 0.85 nm, which is similar to the reported data for LDH intercalated with NO₃⁻ ions⁵⁷. A (002) diffraction peak of Gr appears in the Gr/LDH composite. These phenomena verify the successful deposition of LDH nanoflakes on the surface of Gr nanosheets. After being loaded with corrosion inhibitors (MBT), the d_{003} values of both LDH and Gr/LDH increase to around 1.61 nm, which indicates that the large-sized MBT⁻ ions are successfully intercalated^{58,59}.

Figure 4b shows the FTIR spectra of the different powder samples. Gr hardly has any IR adsorption peaks because it lacks active functional groups and has symmetrical C–C bonding⁶⁰. Similar to LDH, Gr/LDH also clearly shows adsorption peaks at 3450 and 1378 cm⁻¹, which are assigned to the O–H stretching vibration of the hydroxyl group in the interlayer water molecules and the stretching vibration of intercalated NO₃⁻, respectively. For the LDH@MBT and (Gr/LDH)@MBT samples, there are a series of weak characteristic peaks at 730–790, 1280–1460, and 2750–3100 cm⁻¹ corresponding to the stretching vibrations of C–S, C–N–H group and phenyl ring C–H, respectively, indicating that MBT inhibitor is successfully loaded⁶¹.

In the Raman spectra of Gr and Gr/LDH (Fig. 4c), the three distinct peaks at 1350 cm⁻¹, 1580 cm⁻¹, and 2700 cm⁻¹ can be assigned to the D, G, and G' bands of graphene materials, respectively⁶². The peak at 672 cm⁻¹ is assigned to bonds in LDH.

The mass loss of Gr/LDH ranging from 120 °C to 470 °C (Fig. 4d) is due to the release of the interlayer water, the dehydroxylation of the basal layers, and the decomposition of the nitrate anions, which is consistent with the weight change of LDH⁶³. The mass loss of (Gr/LDH)@MBT and LDH@MBT in the range of 200–280 °C is caused by the decomposition of MBT⁶⁴. The MBT loading amounts of LDH and Gr/LDH micro/nano-containers determined from the TG curves are 9.41 wt% and 12.58 wt%, respectively. In addition, the mass loss of Gr and Gr/LDH after 650 °C is caused by the thermal decomposition of graphene^{49,50}.

Figure 5 shows the XPS survey spectra of Gr and Gr/LDH. The existence of the O1s peak (532.5 eV) is due to the weak adsorption of oxygen-containing groups (–OH) on the surface of Gr⁶⁵. The weak adsorption is merely physical and does not alter the hybridization form of carbon atoms⁶⁶. Compared with Gr, the XPS spectrum of Gr/LDH not only exhibits C1s peak and O1s peak but also shows two featured peaks of the deposited CoFe–LDH at 707 eV and 794 eV, which are attributed to Fe2p and Co2p, respectively⁶⁷. The high-resolution C1s spectra of Gr contain two types of carbon bonds: the sp² carbon peak centered at 284.6 eV and the π–π* shake-up peak at 291.7 eV⁶⁸. In contrast, the high-resolution C1s spectra of Gr/LDH show two peaks at 285.5 eV and 286.3 eV, which correspond to sp³ C and C–O bonds⁶⁹. The appearance of sp³ C and C–O bonds confirms the interaction between Gr and LDH.

Supplementary Fig. 4 displays the release curves of MBT from LDH@MBT and (Gr/LDH)@MBT in 3.5% wt% NaCl solution with different pH values. Results show that both LDHs and Gr/LDH micro/nano-containers exhibit different release behaviors of MBT under pH values of 3, 7, and 11, respectively. At pH = 3, the rapid and significant release of MBT is mainly due to the dissociation of LDHs. At pH 7 and 11, the release behavior depends on the exchange of interlayer anions MBT⁻ with chloride ions in the solution. Therefore, when the corrosive medium is initially diffused but has not yet caused a corrosion reaction, the inhibitor MBT⁻ is released by exchanging with corrosive chloride ions. But when the subsequent

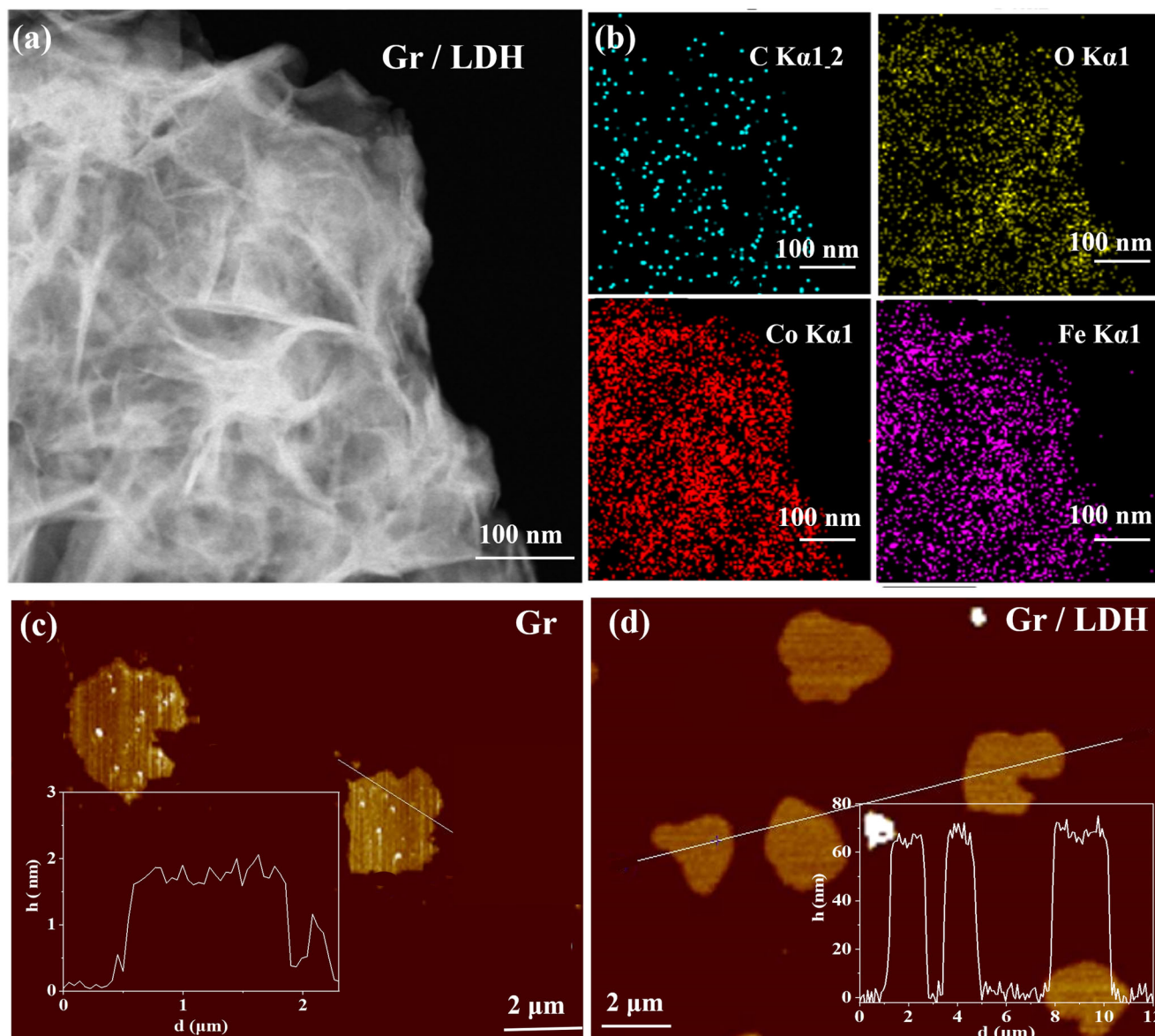


Fig. 3 | Surface morphology analysis of samples. a, b HRTEM images and corresponding elemental mapping analysis of Gr. **c, d** AFM images (inset is thickness attribution) of Gr and Gr/LDH.

electrochemical corrosion reactions cause a local pH drop, the layered structure of LDHs will collapse, which makes large amounts of inhibitors rapidly released.

Supplementary Fig. 5 shows XRD patterns of LDH@MBT and (Gr/LDH)@MBT after immersed in 3.5% wt% NaCl solution. The result shows that the interlayer spacing of LDH@MBT and (Gr/LDH)@MBT decreases and the corresponding 2θ value of (003) and (006) crystallographic plane increases when MBT^- is replaced by Cl^- , which is consistent with the literature⁷⁰.

The MBT loading amounts of LDHs and Gr/LDH micro/nano-containers determined from the above release curves after 7 days of immersion are as high as 8.82 wt% in LDH@MBT and 13.16 wt% in (Gr/LDH)@MBT, which is consistent with the results determined from the TG curves. The high loading capacity of Gr/LDH is related to its own rough morphology. Predictably, the Gr/LDH micro/nano-containers have combined advantages of the physical barrier property (Gr and LDH), the on-demand release of inhibitors, and the uptake of chlorides (LDH), which ensures the passive and active protecting capabilities of coatings.

Corrosion protection properties of micro/nano-containers-embedded coatings

To objectively and directly evaluate the protective performance of the obtained PVB coatings, optical photos of scratched and intact samples immersed in 3.5 wt% NaCl solution were taken, respectively, as shown in Fig. 6 and Supplementary Fig. 6. For the pure PVB sample (Fig. 6a and Supplementary Fig. 6a), after only 3 days of immersion, obvious corrosion products aggregated around the scratch, and the corrosion continued to intensify during the whole immersion period. This indicates that the undoped PVB coating cannot effectively prevent corrosive mediums from penetrating the surface of the metal substrate because of the poor barrier property. Similarly, as shown in Fig. 6b, c, PVB/Gr and PVB/LDH samples also exhibit poor corrosion protection ability. This is related to the uneven dispersion of graphene or LDH in PVB resin, which will be discussed in more detail in a later section. As to PVB/(Gr/LDH) sample (Fig. 6d), although pitting corrosion occurs after immersion of 30 days, the corrosion product accumulation is significantly decreased. The above results confirm that the PVB coatings lacking corrosion inhibitors cannot provide long-term corrosion protection for metal substrates.

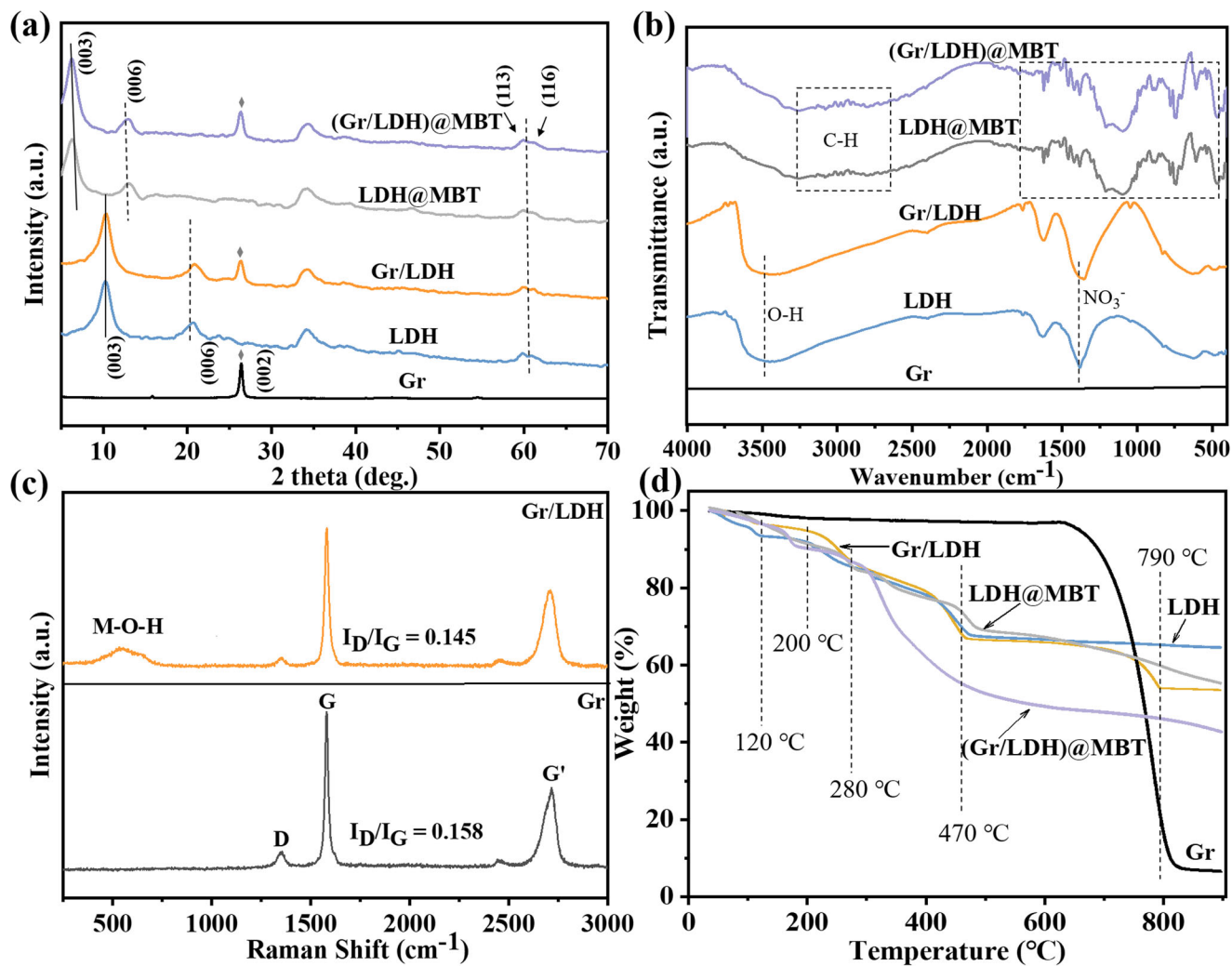


Fig. 4 | Structures of different micro/nano-containers. a XRD patterns, b FTIR spectra, c Raman Spectroscopy, and d TG curves.

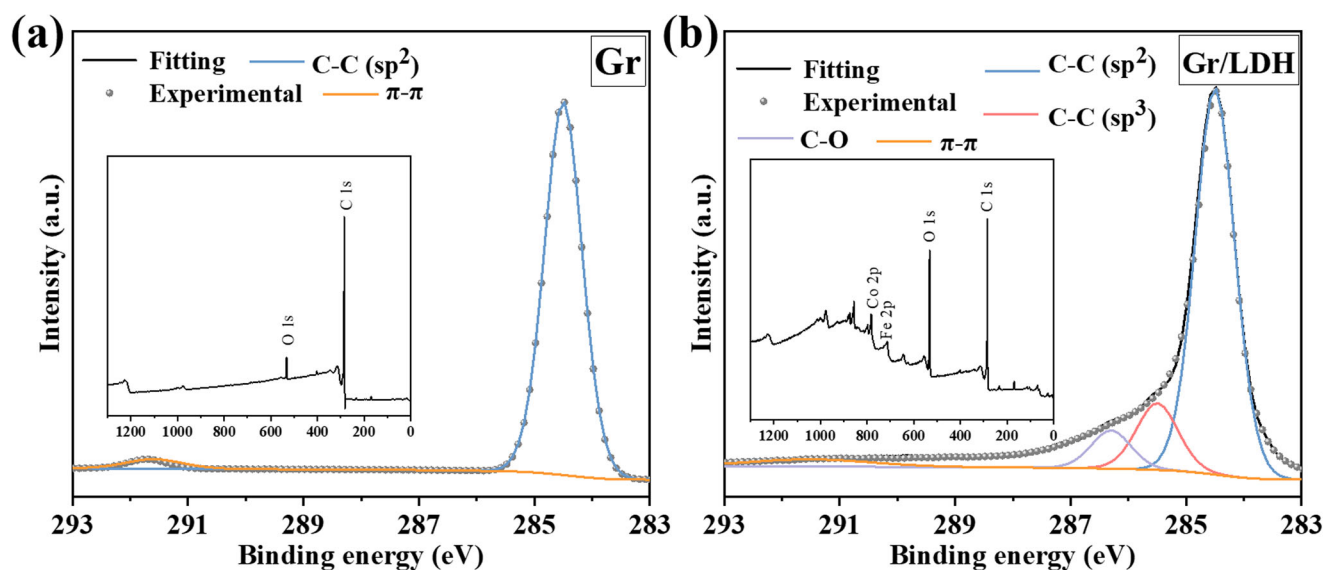


Fig. 5 | XPS spectra. C1s spectra of a Gr and b Gr/LDH, insets: corresponding survey XPS spectra.

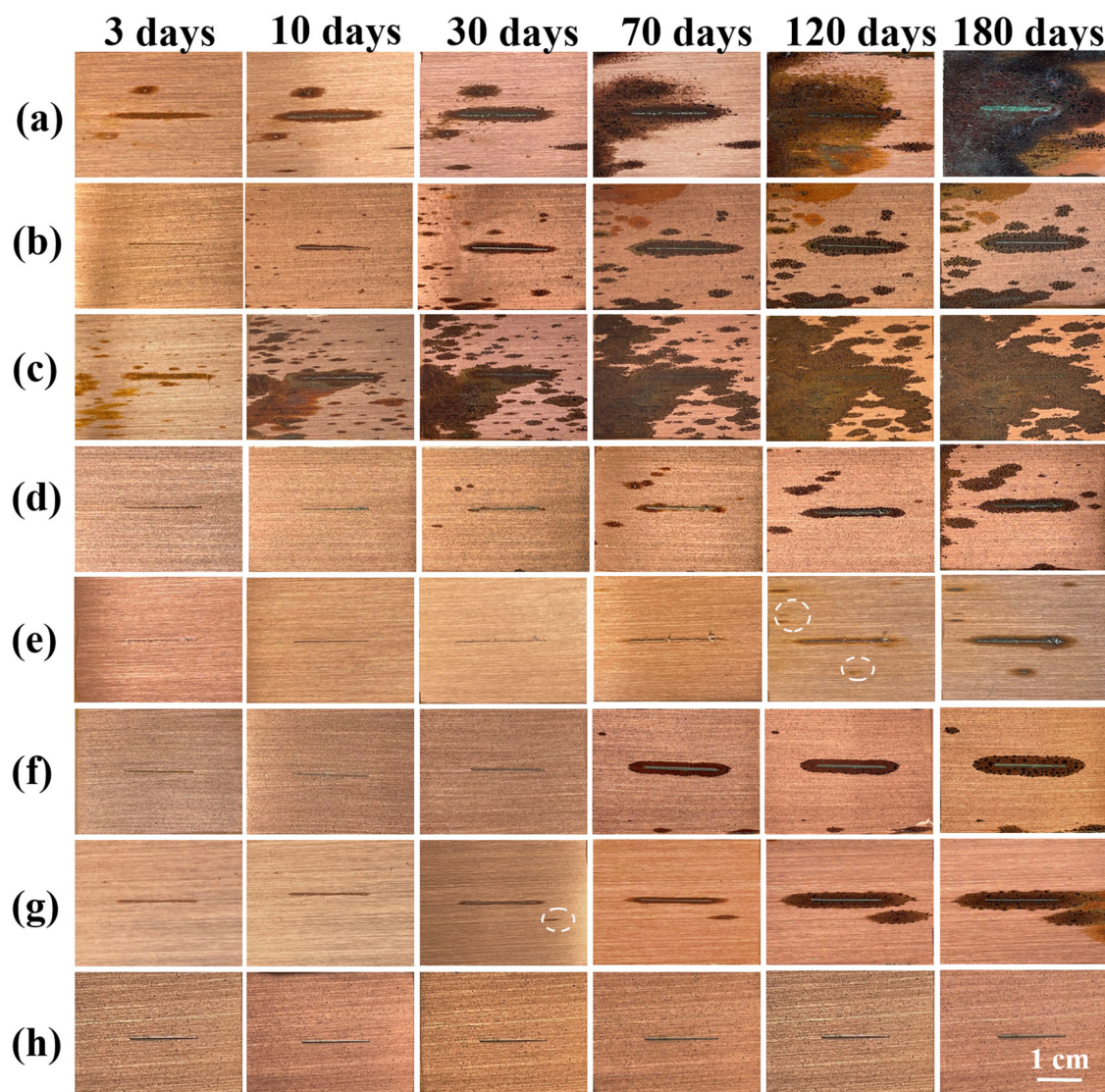


Fig. 6 | Optical images of the scratched coatings on pure copper immersed in 3.5 wt% NaCl solution during 180 days. **a** Pure PVB, **b** PVB/Gr, **c** PVB/LDH, **d** PVB/(Gr/LDH), **e** PVB/MBT, **f** PVB/Gr@MBT, **g** PVB/LDH@MBT, **h** PVB/(Gr/LDH)@MBT.

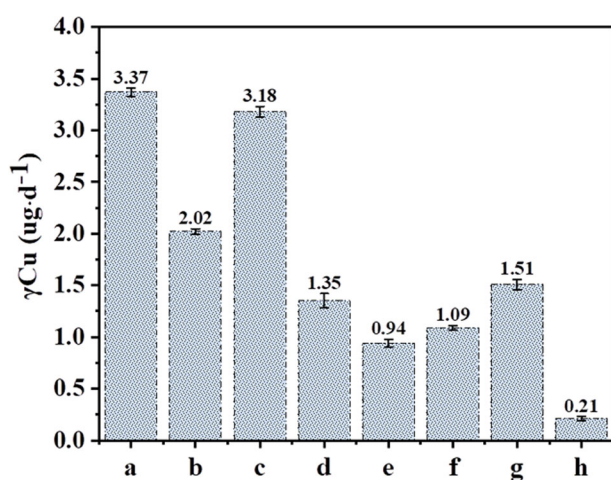


Fig. 7 | Copper ion dissolution rates measured after the scratched samples were immersed in 3.5 wt% NaCl solution for 180 days. (Mean \pm standard deviation). **a** Pure PVB, **b** PVB/Gr, **c** PVB/LDH, **d** PVB/(Gr/LDH), **e** PVB/MBT, **f** PVB/Gr@MBT, **g** PVB/LDH@MBT, **h** PVB/(Gr/LDH)@MBT.

Incorporation of corrosion inhibitors into the PVB coatings can indeed improve the corrosion resistance of copper substrates. However, for PVB/MBT, PVB/(Gr@MBT), and PVB/(LDH@MBT) samples (Fig. 6e–g), after 120 days of immersion, corrosion products began to extend and accumulate around the scratch. PVB/(Gr/LDH@MBT) exhibits the best protection performance among all samples, and no rust spots are visible on the copper surface even after 180 days immersion (Fig. 6h). In addition, observation on intact coating samples during the whole immersion test is consistent with that on the artificially scratched coatings, and PVB/(Gr/LDH@MBT) still has no obvious corrosion after immersion for 180 days (Supplementary Fig. 6h).

The excellent corrosion protection performance of the PVB coatings doped with Gr/LDH composite pre-capsulated with MBT is also evidenced by the copper ion dissolution test of defected samples. The copper dissolution rate significantly decreases from $3.37 \mu\text{g d}^{-1}$ on pure PVB to 2.02, 3.18, 1.35, 0.94, 1.09, 1.51 and $0.21 \mu\text{g d}^{-1}$ on coatings doped with Gr, LDH, Gr/LDH, MBT, Gr@MBT, LDH@MBT, (Gr/LDH)@MBT, respectively (Fig. 7). After the PVB coating being doped with (Gr/LDH)@MBT, its copper ion dissolution rate declines by about 94%.

Supplementary Fig. 7 displays SEM images and EDS analysis of scratched coatings on pure copper immersed in 3.5 wt% NaCl solution for 180 days. It can be seen that all samples except the PVB/(Gr/LDH)@MBT sample have an obvious accumulation of corrosion products in the

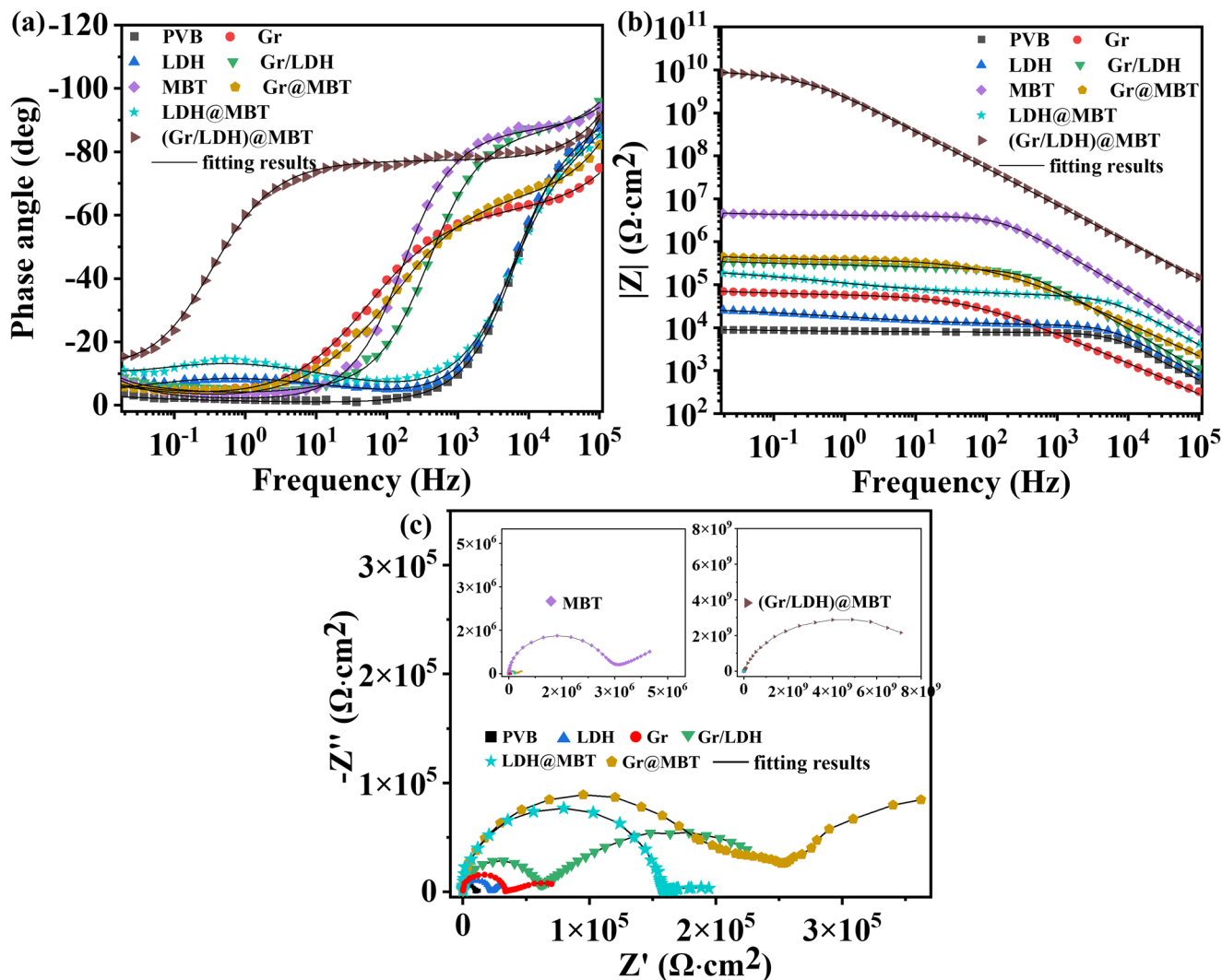


Fig. 8 | EIS results of different coating samples after being immersed in 3.5 wt% NaCl aqueous solution for 180 days. **a** Impedance modulus, **b** phase angle bode plots, and **c** Nyquist diagrams.

scratched area. EDS-mapping results show that Cu and C elements are predominantly detected within and outside the scratch of the PVB/(Gr/LDH)@MBT sample, respectively, indicating that the sample still has good corrosion resistance for up to 180 days of immersion. But for the other samples, element Cu is detected not only within to the scratches but also in the surrounding area. Additionally, as the main component of the coatings, element C shows discontinuous distribution on the surfaces of these samples, which is attributed to the blistering or peeling of coatings and the spreading of corrosion products. The SEM images and EDS-mapping results agree with those of the immersion test.

EIS measurements were used to quantitatively evaluate the corrosion resistance of intact coating samples in 3.5 wt% NaCl solution. Figure 8a–c shows the bode modulus, phase angle plots, and Nyquist diagrams, respectively, of different samples after 180 days of immersion. PVB/(Gr/LDH)@MBT sample has the highest impedance values among all intact coating samples, the highest diameter of the semicircle, and the phase angle value of this sample is near -90° in a wide frequency range. This result indicates that the PVB/(Gr/LDH)@MBT sample still maintains its excellent barrier property after immersion for up to 180 days.

As shown in Fig. 9a, except for the PVB/(Gr/LDH)@MBT sample, the low-frequency impedance modulus ($|Z|_{lf}$ at 0.01 Hz) values of other samples present a continuous decreasing tendency during the whole test period, reflecting the gradual deterioration of barrier performance of the coatings. The $|Z|_{lf}$ of PVB/(Gr/LDH)@MBT sample exhibits the highest value and

maintains a stable value of around $10^{10} \Omega \text{ cm}^2$ over the whole immersion of 180 days. EIS data were also fitted by ZView software using proper equivalent electrical circuits (EECs), as shown in Fig. 9b. Here, R_s , C_c , R_{po} , C_{dl} , R_{ct} , and Z_w denote solution resistance, coating capacitance, electrolyte resistance in micropores of the coating, double-layer capacitance, charge transfer resistance, and Warburg-diffusion impedance, respectively. When conducting fitting work, all capacitance elements were replaced with constant phase angle elements (CPEs)⁷¹. The impedance of a CPE is defined by the following equation:

$$Z_{CPE} = \frac{Y_0^{-1}}{(j\omega)^n} \tag{5}$$

Where Y_0 is the magnitude of the CPE, ω is the angular frequency, and n refers to the dimensionless index. C_c and C_{dl} were calculated from the following Eqs. 6 and 7, respectively^{72,73}:

$$C_c = Y_0^{\frac{1}{n}} \cdot \left(\frac{R_s \cdot R_{po}}{R_s + R_{po}} \right)^{\frac{1-n}{n}} \tag{6}$$

$$C_{dl} = Y_0^{\frac{1}{n}} \cdot \left(\frac{R_s \cdot R_{ct}}{R_s + R_{ct}} \right)^{\frac{1-n}{n}} \tag{7}$$

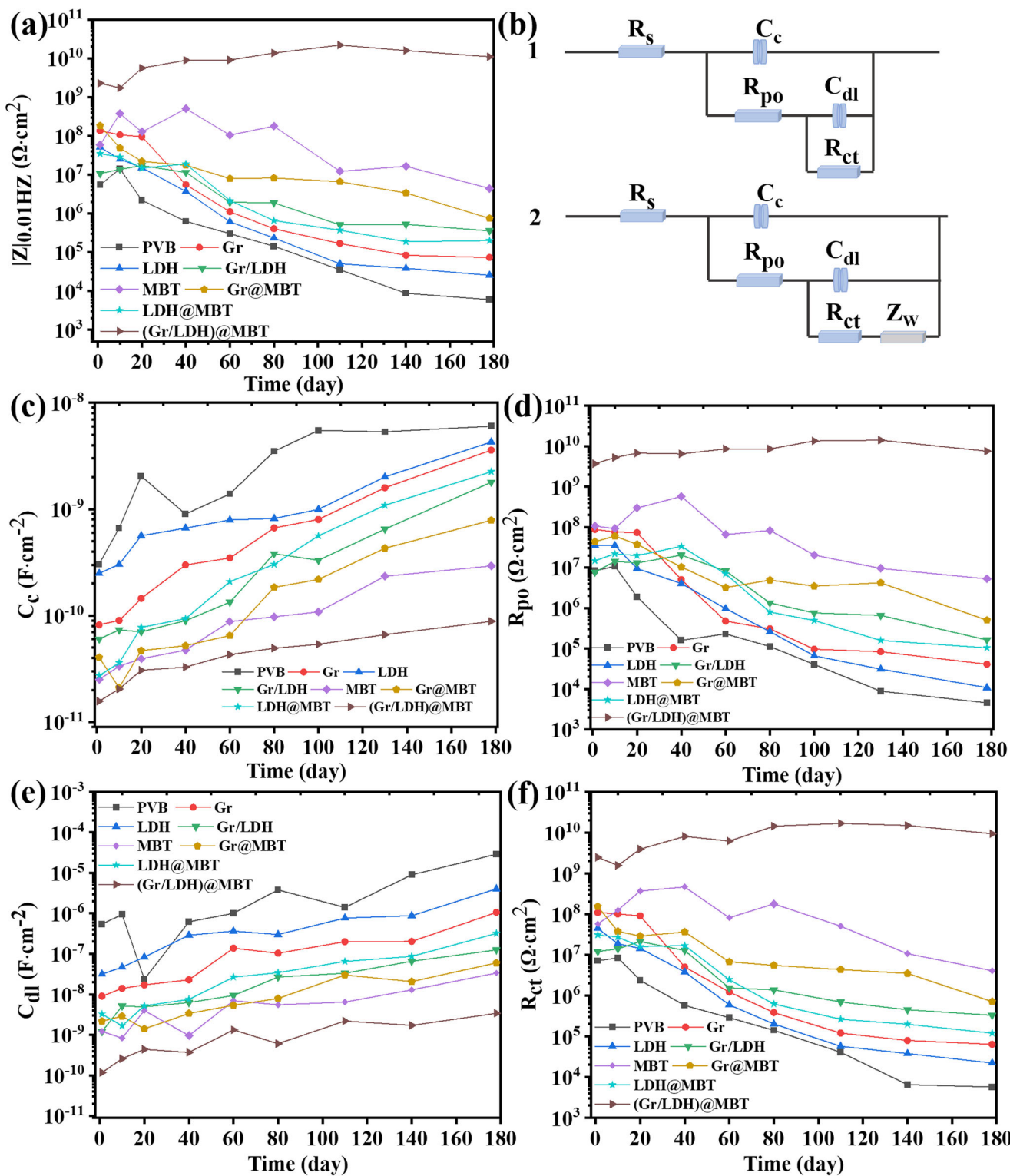


Fig. 9 | Analysis of EIS results. a Evolution of low-frequency impedance modules (measured at 10 mHz) of intact coatings with immersion time in 3.5 wt% NaCl aqueous solution. **b** Equivalent electrical circuit models for PVB coatings on pure copper. **c–f** Variations of C_c , R_{po} , C_{dl} , and R_{ct} during the whole testing time.

Fitting parameters are shown in Supplementary Tables 1 and 2. The Chi-square values of all samples range from 10^{-4} to 10^{-3} , and all the fitting errors are less than 5%. These results indicate that the selected EECs are appropriate and reliable. It is well known that C_c is commonly used to evaluate the water uptake in polymer coatings. Usually, a lower C_c value means better water impermeability and lower water uptake. Figure 9c shows

that the pure PVB coating presents the highest C_c value and the lowest R_{po} value among all samples during the whole period of 180 days of immersion, showing that this coating has the worst physical barrier performance. This phenomenon implies that corrosive medium water can easily penetrate into the un-doped PVB coating through internal defects. PVB/(Gr/LDH) sample has lower C_c and higher R_{po} values than pure PVB, PVB/Gr, and PVB/LDH

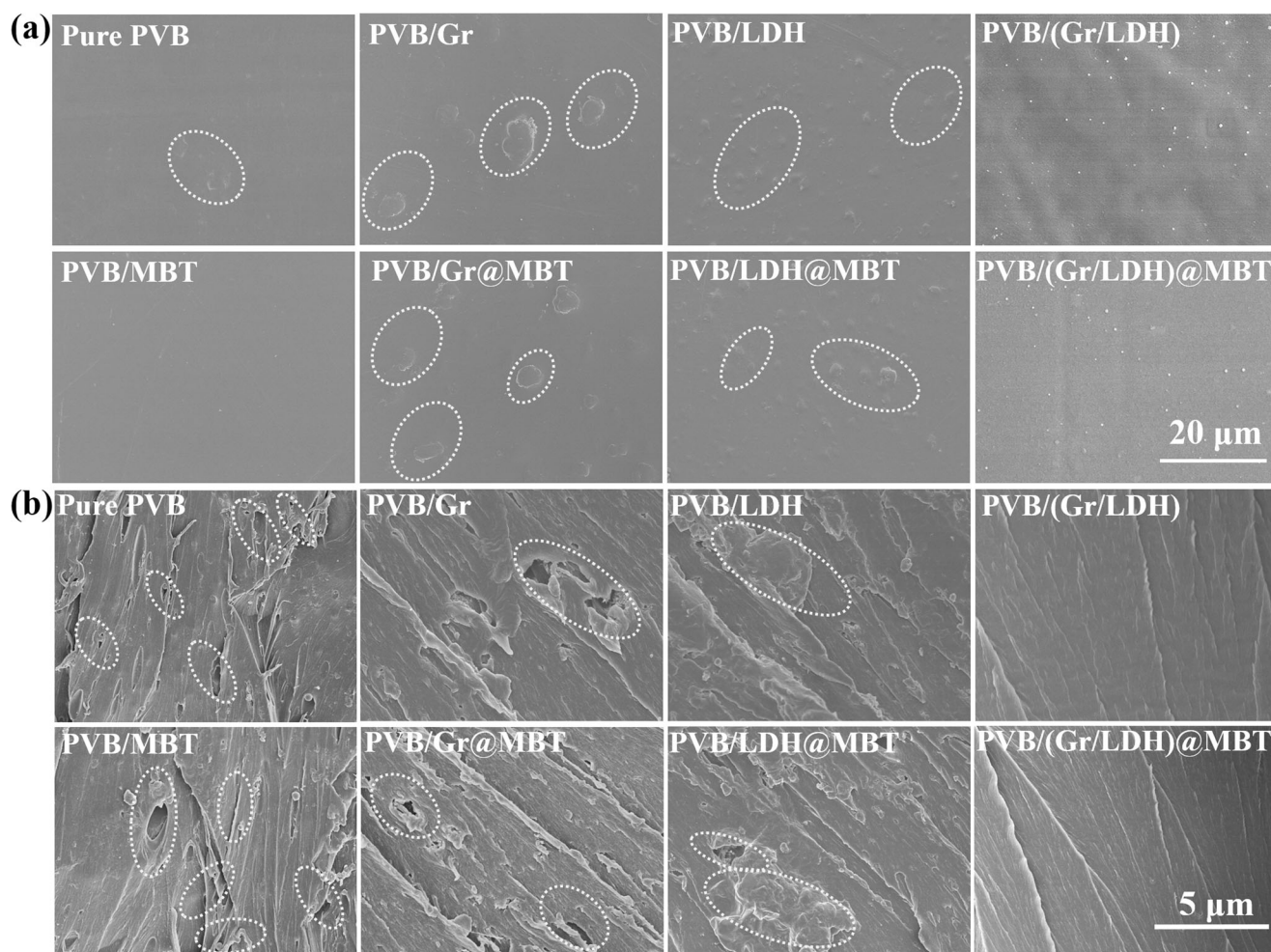


Fig. 10 | SEM images of coatings. Top-view **a** and cross-section. **b** SEM images of different coatings.

samples, which suggests that the addition of Gr/LDH composite micro/nano-containers can be a better remedy for internal defects of PVB coating (Fig. 9d). After 180 days of immersion in 3.5 wt% NaCl solution, the PVB coating embedded with (Gr/LDH)@MBT still maintains the highest value of R_{po} and the lowest value of C_c , manifesting that this coating has the best impermeability to corrosive medium water.

C_{dl} is commonly used to estimate the number of active corrosion sites in metal/electrolyte interfaces. In general, the active protecting performance of a coating is evaluated by the values of its C_{dl} and R_{ct} . As shown in Fig. 9e, the C_{dl} values of different samples during the middle and later stages of the experiment are arranged as follows: PVB > PVB/LDH > PVB/Gr > PVB/(LDH@MBT) > PVB/(Gr/LDH) > PVB/(Gr@MBT) > PVB/MBT > PVB/(Gr/LDH@MBT). For R_{ct} values (Fig. 9f), the order is reversed. The R_{ct} and C_{dl} values of PVB, PVB/Gr, PVB/LDH, and PVB/(Gr/LDH) samples keep falling and rising, respectively, which demonstrates that the corrosion progress in meta/coating interface cannot be inhibited due to the lack of corrosion inhibitors. MBT-containing coatings have higher R_{ct} values than MBT-free coatings. As expected, the PVB/(Gr/LDH@MBT) sample displays the highest R_{ct} and the lowest C_{dl} values among all samples, and R_{ct} of this sample presents a rising tendency over the whole immersion of 180 days, indicating a continuous ‘self-healing’ effect.

Discussion

The PVB coatings encapsulated with Gr/LDH micro/nano-containers exhibit satisfactory corrosion performance, which is the result of their passive and active protecting capabilities. Generally, the corrosion procedure can be divided into two main stages, involving the initial infiltration

and diffusion process of corrosive medium (such as Cl^- , H_2O , and O_2) in the coating matrix and the following corrosion reaction stage at the metal/coating interface.

The passive protection performance of a coating, which depends on the barrier ability against the penetration of corrosion ions, is of vital importance in the first stage. For container-based coatings, their barrier properties are mainly determined by two factors: one is the dispersion quality of micro/nano-containers in the coating matrix, and another is the physical shielding abilities of the doped micro/nano-containers themselves.

Top-view SEM images of different PVB coatings are shown in Fig. 10a. It can be clearly seen that the Gr or Gr@MBT nanosheets severely aggregate in PVB resin, which is attributed to the strong van der Waals forces among Gr nanosheets⁷⁴. Similarly, the uneven distribution and obvious aggregation of LDH or LDH@MBT nanoparticles are also observed on the surface of PVB/LDH or PVB/(LDH@MBT), respectively, which is caused by the formation of intermolecular hydrogen bonds between different LDH nanoflakes. However, Gr/LDH or (Gr/LDH)@MBT composites are well-distributed in PVB resin, indicating their excellent compatibility with PVB coatings. This result is attributed to the fact that LDH nanoflakes grow vertically and uniformly on both sides of Gr (Fig. 2b), which not only weakens van der Waals forces among Gr sheets but also avoids the self-agglomeration of LDH. In addition, the resulting Gr/LDH composite has a larger contact area with PVB resin, so there are more hydrogen bonds between the deposited LDH nanoflakes and the resin backbone, which can improve their compatibility.

As shown in Fig. 10b, numerous micro-pores are observed inside the pure PVB and PVB/MBT samples due to the fast evaporation of solvent

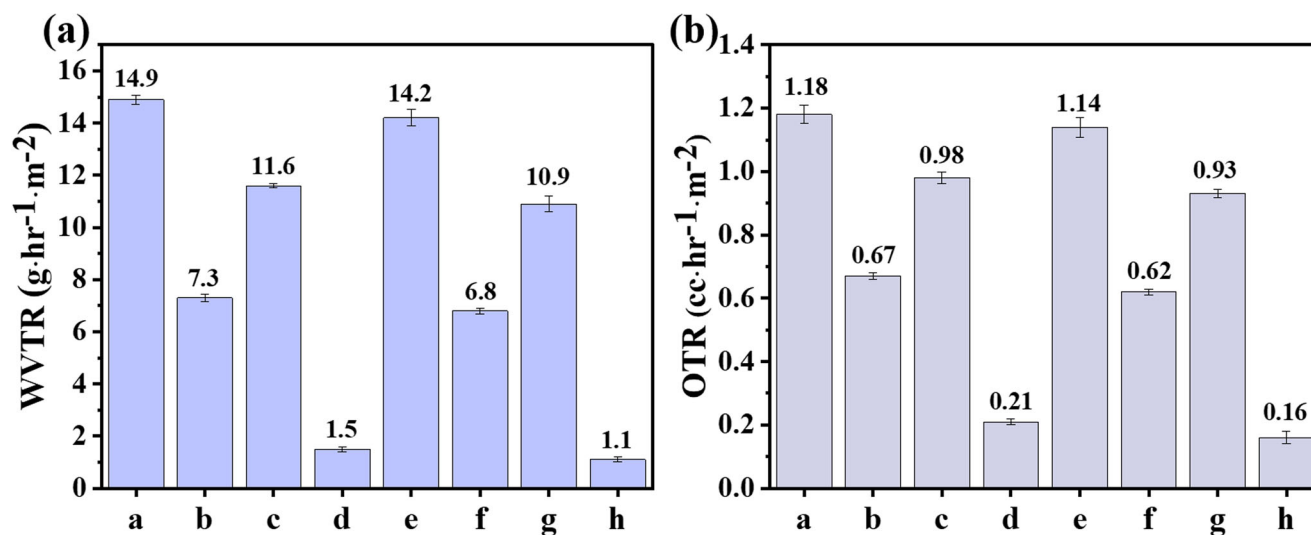


Fig. 11 | WVTR and OTR of different coatings. (Mean ± standard deviation). a PVB, b PVB/Gr, c PVB/LDH, d PVB/(Gr/LDH), e PVB/MBT, f PVB/Gr@MBT, g PVB/LDH@MBT, h PVB/(Gr/LDH@MBT).

during the curing process, which means that corrosive medium can diffuse and penetrate through holes and cracks quickly. Incorporating micro/nano-containers in the PVB matrix can curb the abovementioned phenomenon, but defects or holes are still noticeable in PVB/Gr, PVB/LDH, PVB/Gr@MBT, and PVB/LDH@MBT coatings. Agglomerated micro/nano-containers are found inside these coatings, which is consistent with the results of top-view SEM images. The cross-section morphology of PVB/(Gr/LDH@MBT) is dense and free of visible cracks and holes, indicating superior barrier qualities. This phenomenon also demonstrates the good compatibility of Gr/LDH micro/nano-containers with PVB coatings.

The particle size of micro/nano-containers has a great influence on the protective properties of coatings. The particle sizes of Gr, LDH, and Gr/LDH powder fall within the range of 750–4100 nm, 1200–3500 nm, and 900–2300 nm, respectively (supplementary Fig. 8a). The particle size of Gr/LDH has an average of 1470 nm, which is smaller compared to the average particle size of Gr (1700 nm) and LDH (1980 nm). The particle size distributions of the three samples (Gr, LDH, and Gr/LDH) in water, methanol, and PVB/methanol are shown in Supplementary Figs. 8b–d. It is evident that Gr/LDH exhibits the narrowest particle size distribution and the smallest average size in every liquid phase.

The sedimentation behavior of different micro/nano-containers in resin solution is studied during aging. After only 7 days, serious sedimentation is observed on PVB solution doped with LDH micro/nano-containers, regardless of the encapsulation of MBT (Supplementary Figs. 9e, f). There is no sedimentation phenomenon in PVB solution doped with Gr/LDH and (Gr/LDH)@MBT composites (Supplementary Figs. 9g, h) even after 300 days. This result also confirms the excellent dispersibility of Gr/LDH. But this work and the related literature cannot accurately explain at this stage why Gr/LDH is well dispersed⁷⁵. The reason why the prepared Gr/LDH composites can interact well with the polymeric chains of coating will be the focus of future research.

The physical shielding abilities of Gr/LDH composite micro/nano-containers highly depend on the synergistic barrier functions provided by Gr and LDH. The values of WVTR and OTR can intuitively reflect the barrier performance of PVB coatings to resist the infiltration and diffusion of H₂O and O₂, as shown in Fig. 11. Compared with blank PVB coating, the (Gr/LDH)@MBT-doped PVB coating has a decrease of 91.3% and 68.5% in WVTR and OTR values, respectively, which makes the biggest decline among all coatings in this work. The WVTR and OTR values of Gr- or LDH-doped PVB coatings are slightly lower than those of blank PVB coating but much higher than those of PVB coating incorporated with Gr/LDH micro/nano-containers. In addition, there is no significant difference

Table 1 | Results of elemental analysis by CHN mode

Sample name	C/wt%	H/wt%	N/wt%	MBT/wt%
Gr	98.74	0.12	0.028	
Gr@MBT	99.16	0.15	0.097	0.83

in OTR and WVTR values of these micro/nano-containers before and after loading corrosion inhibitors. The above results are consistent with those of R_{po} and C_c , both indicating that although the addition of traditional graphene or LDH nanosheets cannot effectively improve the barrier performance of PVB coatings, the Gr/LDH composite obtained by combining the traditional Gr and LDH by EAT endow PVB coatings with superior barrier performance. Therefore, the excellent shielding properties of Gr/LDH micro/nano-containers themselves, as well as their uniform dispersibility in PVB resin, interpret the greatly improved passive protecting capability of the (Gr/LDH)-doped PVB coatings.

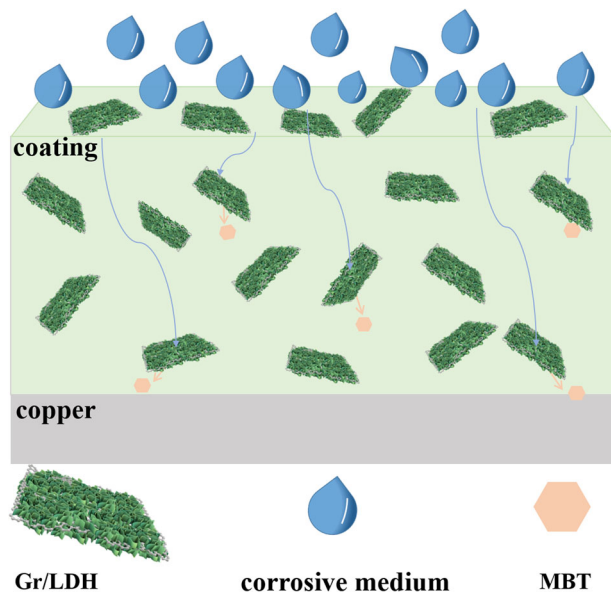
The active protecting performance of a coating, which depends on the on-demand release of corrosion inhibitors from the doped micro/nano-containers, is crucial in the following corrosion reaction stage. In fact, during the gradual diffusion of the aggressive mediums to the metal surface, the doped (Gr/LDH)@MBT composites rely on their ion-exchange properties to release inhibitors while capturing the corrosion ions such as Cl⁻ and SO₄²⁻. Furthermore, once corrosive mediums inevitably reach the copper/coating interface, inhibitors (MBT) are timely released from Gr/LDH micro/nano-containers triggered by pH changes of the local corrosion area to form protective layers on the metal surface. Therefore, the corrosion reaction is inhibited in a short time.

The loading amounts of corrosion inhibitors in micro/nano-containers also have a great effect influence on the active protection properties of coatings. In fact, MBT can be not only intercalated into the interlayer of LDH but also adsorbed on the surface of LDH and Gr⁷⁶. Table 1 shows the elemental analysis results, and it can be calculated that the MBT loading amount of Gr is only 0.83 wt%, suggesting low adsorption of MBT on Gr. Therefore, the high loading amount of MBT should be attributed to the special structure of Gr/LDH. Supplementary Fig. 10 shows the nitrogen adsorption–desorption isotherms of LDH and Gr/LDH. The BET surface area of LDH and Gr/LDH was measured to be 46.12 m² g⁻¹ and 96.58 m² g⁻¹, respectively. The larger BET surface area endows micro/nano-containers with higher MBT-loading capability.

In addition, the superior anti-corrosive performance of the PVB/(Gr/LDH@MBT) sample should be traced to the method for preparing free-

Table 2 | Results of elemental analysis by O mode

Sample name	C/wt%	O/wt%
Gr	98.76	0.92
GO	62.72	33.58
rGO	81.53	17.84

**Fig. 12 | Anticorrosion mechanism.** Schematic illustration of self-healing effect of the coatings doped with Gr/LDH micro/nano-containers.

standing Gr/LDH nanosheet using EAT. The O content of graphene used in this study is 0.92% (Table 2), which is much lower than that in graphene oxide (33.58%) and reduced graphene oxide (17.84%). Moreover, graphene was also employed to prepare Gr/LDH composite by hydrothermal methods. The corresponding SEM images were added in supplementary Fig. 11. SEM images show that there are no LDHs nanoflakes on the surface of the graphene nanosheet. Therefore, such a low content of O can not play a major role in the stabilization of the graphene particles in an aqueous solution and act as nucleation sites for the precipitation reactions and formation of LDHs. The core of the electrochemically assisted deposition technique (EAT) is the efficient electron transfer between the working electrode and the graphene nanosheet. These results prove that EAT provides the sustained driving force for the deposition of LDH, which ensures the dense, uniform, and strongly adherent growth of LDH nanoflakes on the surface of Gr. Thus, the obtained Gr/LDH micro/nano-container can be loaded with corrosion inhibitors in high amounts.

For the purpose of comparison, GO/LDH micro/nano-containers were also prepared by traditional hydrothermal method. SEM and AFM images (Supplementary Fig. 12) show that the dispersion of LDHs nanoflakes on the surface of the graphene nanosheet is non-uniform, which may be related to the alkalinity of the whole solution during preparation. The thickness of the resulting LDHs nanoflakes is limited due to the lack of a continuous driving force for the growth of LDHs nanoflakes (Supplementary Fig. 12c, d). In addition, the WVTR and OTR values of PVB/(GO/LDH) coatings are about 3.3 and 2.8 times than those of PVB/(Gr/LDH) coatings, respectively (Supplementary Fig. 13). As shown in Supplementary Figs. 14 and 15, for the copper substrate coated with PVB/(GO/LDH@MBT) coatings, obvious corrosion products accumulate after 80 days of immersion. All the above results indicate that the Gr/LDH micro/nano-containers prepared by EAT can impart polymer coatings with better protective

performance compared to GO/LDH micro/nano-containers synthesized by traditional hydrothermal method.

Based on the above analysis, a possible protection mechanism of Gr/LDH micro/nano-containers is illustrated in Fig. 12. The Gr/LDH micro/nano-container exhibits a sandwich structure, with dense LDHs nanoflakes on both lower and upper surfaces of inert Gr. Gr/LDH exhibits larger pore volume and pore size, which not only ensure the loading amount of MBT but also reduce its diffusion resistance. On one hand, graphene nanosheets and LDHs nanoflakes synergistically build a 'labyrinth effect' inside the coating, further lengthening the diffusion path of corrosive mediums, such as Cl^- , H_2O , and O_2 . On the other hand, as aggressive ions diffused into the coating/metal interface, corrosion inhibitors can be released from the interlayer galleries of LDHs and impede the corrosion of metal substrate by substituting the aggressive ions.

In summary, Gr/LDH micro/nano-container was synthesized by electrochemically assisted sol-gel deposition technique (EAT). The obtained Gr/LDH composite has a sandwich-like nanostructure: Gr nanosheet is the middle layer of this structure, while LDHs nanoflakes with thicknesses up to ~ 70 nm are uniformly covered on both the upper and lower surfaces of the Gr nanosheet. The PVB coatings (10–14 μm) embedded with MBT-encapsulated Gr/LDH micro/nano-containers exhibit excellent passive and active protecting capabilities and can still protect copper substrates from corrosion after being immersed in 3.5 wt% NaCl solution for more than 180 days. EAT solves the problem that LDHs nanoflakes tend to self-agglomerate during nucleation and growth and makes it possible to use inert graphene (rather than graphene oxide) as the substrate to prepare Gr/LDH composite.

Methods

Materials and chemicals

Graphene was obtained from XFNANO (Nanjing XFNANO Technology Co., Ltd., China). Cobaltous nitrate hexahydrate ($\text{CoNO}_3 \cdot 6\text{H}_2\text{O}$, AR), ferric nitrate nonahydrate ($\text{Fe}(\text{NO}_3)_3 \cdot 9\text{H}_2\text{O}$, AR), sodium nitrate (NaNO_3 , AR), ethanol (AR) and methanol (AR) were purchased from Aladdin. 2-Mercaptobenzothiazole (MBT, 98%), sodium chloride (NaCl, AR), and polyvinyl butyral (PVB, 15.0–18.0 mPa.s, butyral 70–75%) were obtained from Sinopharm Chemical Reagent (Beijing Co. Ltd.). Pure copper sheets (supplied by Quanfu Metal Co., Ltd., China) were cut to 40 mm \times 25 mm with a thickness of 1.5 mm.

Electrosynthesis of Gr/LDH and LDH micro/nano-containers

The electrodeposition process was conducted in a three-electrode cell using a CHI 760E potentiostat (Chenhua Co., Ltd., China). The electrolyte contained 100 mL H_2O , 0.85 g NaNO_3 , 1.46 g $\text{CoNO}_3 \cdot 6\text{H}_2\text{O}$, and 0.61 g $\text{Fe}(\text{NO}_3)_3 \cdot 9\text{H}_2\text{O}$. To obtain a homogeneous suspension, 80 mg graphene was ultrasonicated and dispersed in the above solution. The electrodeposition was performed by chronoamperometry measurement with deposition potential ranging from -0.7 to -1.3 V (vs. Ag/AgCl), and deposition time varied from 10 to 40 min. Thereafter, the solution was centrifuged at 8000 rpm for 10 min and washed with deionized water three times. The products were then vacuum dried at 80 $^\circ\text{C}$ for 6 h and named Gr/LDH. Similarly, the LDH nanosheets were prepared through the same electrodeposition process without the addition of graphene.

Loading of MBT inhibitors

In total, 300 mg Gr/LDH or LDH was added to the 0.1 M MBT-containing solution (pH = 9) and left under stirring for 24 h. The products were obtained by centrifugation at 10,000 rpm for 20 min and further drying for 8 h and were named (Gr/LDH)@MBT or LDH@MBT, respectively.

Preparation of PVB coating systems

For comparison, eight different coatings were prepared, including pure PVB, PVB/Gr, PVB/LDH, PVB/MBT, PVB/(Gr@MBT), PVB/(LDH@MBT), PVB/(Gr/LDH@MBT). 45 mg micro/nano-containers that had been ground in a ball mill were mixed with 3 g PVB powder in 30 mL

methanol and agitated vigorously for 12 h. The treated PVB was dip-coated on a pure copper surface (4 cm × 2 cm × 0.1 cm) by a dip-coater with a pulling rate of 0.5 cm/min. The coated copper substrates were cured at 45 °C in an oven for 36 h. The cured coating thickness was measured as 16 ± 2 μm by an eddy-current coating thickness gauge (Qnix 8500, Germany).

Instruments and characterizations

The shapes, morphologies, and structures of micro/nano-containers and coatings were observed by transmission electron microscopy (TEM, HT-7700, Hitachi, Japan), scanning electron microscopy (SEM, SU 8010, Hitachi, Japan), high-resolution transmission electron microscopy (HRTEM, JEM 2100 F, JEOL, Japan), atomic force microscopy (AFM, Multimode 8, Bruker, Germany). The crystal and chemical structures of micro/nano-containers were analyzed by Fourier transform infrared (FT-IR) spectroscopy (Nicolet 6700, Thermo Scientific, USA), Raman spectroscopy (Lab.HR800, Jobin Yvon, France), thermogravimetric analysis (TGA, STA409PC, METZSCH, Germany), element analysis (Elementar Vario MICRO cube, Germany) and X-ray diffraction (XRD, Rigaku SmartLab, 40 KV, 40 mA) with CuKα radiation. The nitrogen adsorption–desorption tests were performed on Micromeritics ASAP 2020 analyzer. The concentration of MBT inhibitors released from micro/nano-containers in solution was measured by UV–vis spectrometer (TU-1901, PERSEE, China). The water vapor transmission rate (WVTR) of different composite coatings was measured by a Water vapor permeability tester (MOCON).

Corrosion performance evaluation

Electrochemical impedance spectroscopy (EIS) was used to evaluate the corrosion resistance of as-prepared coatings in 3.5 wt% NaCl solution. The measurements were performed on a VersaSTAT 3 F (AMETEK, USA) workstation with a three-electrode system, using an Ag/AgCl (saturated KCl) electrode, a platinum foil electrode, and intact coating samples as reference, counter, and working electrodes, respectively. The EIS data were collected from 100 kHz to 10 mHz with 20 mV amplitude sinusoidal voltage. The edge areas of intact coating samples were sealed with paraffin, and the exposed areas for the EIS test were unified to 2.0 cm × 2.7 cm.

To reduce the time that the immersion test takes, a chloride ion accelerated corrosion test was carried out on the scratched coating samples (defeated size: 0.1 mm × 10 mm) in 3.5 wt% NaCl solution. The number of copper ions dissolved from scratched coating samples was measured by an atomic absorption spectrometer (AA800, PerkinElmer, USA).

Data availability

All data generated or analyzed during this study are included in this published article, and any additional data that support the findings of this study are available from the corresponding author upon reasonable request.

Received: 19 June 2023; Accepted: 18 February 2024;

Published online: 27 February 2024

References

- Biezma, M. V. & San Cristóbal, J. R. Methodology to study cost of corrosion. *Corros. Eng. Sci. Technol.* **40**, 344–352 (2005).
- Ptak, S. & Pomykala, K. Corrosion problems in the refinery industry. *Naft-Gaz.* **4**, 312–323 (2022).
- Aslam, R., Mobin, M., Zehra, S. & Aslam, J. A comprehensive review of corrosion inhibitors employed to mitigate stainless steel corrosion in different environments. *J. Mol. Liq.* **364**, 119992 (2022).
- Salaluk, S. et al. Nanonetwork composite coating for sensing and corrosion inhibition. *Adv. Mater. Interfaces* **7**, 2001073 (2020).
- De, S. & Lutkenhaus, J. L. Corrosion behaviour of eco-friendly airbrushed reduced graphene oxide-poly(vinyl alcohol) coatings. *Green. Chem.* **20**, 506–514 (2018).
- Xu, W. J., Yang, C., Su, W. M., Zhong, N. J. & Xia, X. N. Effective corrosion protection by PDA-BN@CeO₂ nanocomposite epoxy coatings. *Colloids Surf. A* **657**, 130448 (2023).
- Zhao, Z. H. et al. Effect of alpha-Al₂O₃ additive on the microstructure and properties of MAO coatings prepared on low carbon steel. *J. Mater. Res. Technol.* **9**, 3875–3884 (2020).
- Bao, Y., Wei, Y. M. & Fu, R. ZnPA@ZIF-8 nanoparticles: synthesis, sustained release properties and anticorrosion performance. *Colloids Surf. A* **651**, 129776 (2022).
- Fei, W. X. et al. Anti-corrosion and electrically conductive inorganic conversion coatings based on aligned graphene derivatives by electrodeposition. *Nano Mater. Sci.* **4**, 244–250 (2022).
- Taj, M. et al. Anticorrosion and electromagnetic interference shielding performance of bifunctional PEDOT-graphene nanocomposites. *Diam. Relat. Mater.* **132**, 109690 (2023).
- Alao, A. O., Popoola, A. P., Dada, M. O. & Sanni, O. Utilization of green inhibitors as a sustainable corrosion control method for steel in petrochemical industries: a review. *Front. Energy Res.* **10**, 1063315 (2023).
- Ci, X., Zhao, W. & Gao, W. Achieving high loading inhibitor carriers with pH-response for active corrosion protection using attapulgite. *Mater. Today Nano* **19**, 100228 (2022).
- Shchukin, D. G. & Möhwald, H. Self-repairing coatings containing active nanoreservoirs. *Small* **3**, 926–943 (2007).
- Lee, J. & Berman, D. Inhibitor or promoter: Insights on the corrosion evolution in a graphene protected surface. *Carbon* **126**, 225–231 (2018).
- Sun, X. G. et al. A novel coating with SiO₂ anchored on MXene loading tannic acid for self-healing anticorrosive performance. *J. Alloy. Compd.* **928**, 167202 (2022).
- Cai, M. et al. Elucidating the electrochemical mechanism for enhanced corrosion of Ti₃C₂T_x-coated mild steel. *Surf. Topogr. Metrol. Prop.* **9**, 035033 (2021).
- Dowsett, M., Adriaens, A., Schotte, B., Jones, G. & Bouchenoire, L. In-situ spectroelectrochemical study of the growth process of a lead decanoate coating as corrosion inhibitor for lead surfaces. *Surf. Interface Anal.* **41**, 565–572 (2009).
- Dong, Y. H., Wang, F. & Zhou, Q. Protective behaviors of 2-mercaptobenzothiazole intercalated Zn-Al-layered double hydroxide coating. *J. Coat. Technol. Res.* **11**, 793–803 (2014).
- Kumar, S. S., Kakooei, S., Ismail, M. C. & Haris, M. Synthesis and characterization of metal ion end capped nanocontainer loaded with duo green corrosion inhibitors. *J. Mater. Res. Technol.* **9**, 8350–8354 (2020).
- Najmi, P., Keshmiri, N., Ramezanzadeh, M., Ramezanzadeh, B. & Arjmand, M. Design of nacre-Inspired 2D-MoS₂ nanosheets assembled with mesoporous covalent organic frameworks (COFs) for smart coatings. *ACS Appl. Mater. Interfaces* **14**, 54141–54156 (2022).
- Hou, P. M., Liu, C. B., Wang, X. & Zhao, H. C. Layer-by-Layer self-assembled graphene oxide nanocontainers for active anticorrosion application. *Int. J. Electrochem. Sci.* **14**, 3055–3069 (2019).
- Xu, J. B., Cao, Y. Q., Fang, L. & Hu, J. M. A one-step preparation of inhibitor-loaded silica nanocontainers for self-healing coatings. *Corros. Sci.* **140**, 349–362 (2018).
- Liu, T. F. et al. Preparation of highly efficient self-healing anticorrosion epoxy coating by integration of benzotriazole corrosion inhibitor loaded 2D-COF. *J. Ind. Eng. Chem.* **97**, 560–573 (2021).
- Yeganeh, M., Saremi, M. & Rezaeyan, H. Corrosion inhibition of steel using mesoporous silica nanocontainers incorporated in the polypyrrole. *Prog. Org. Coat.* **77**, 1428–1435 (2014).
- Luchkina, V. A. et al. Corrosion inhibition of Mg90 alloy by mixtures based on sodium oleate. Influence of oxide film thickness. *Int. J. Corros. Scale Inhib.* **9**, 1607–1629 (2020).
- Zhang, B. B., Qiao, M. Y., Xu, W. C. & Hou, B. R. All-organic superhydrophobic coating with anti-corrosion, anti-icing capabilities and prospective marine atmospheric salt-deliquesce self-coalesce protective mechanism. *J. Ind. Eng. Chem.* **115**, 430–439 (2022).

27. Cai, H. Y., Wang, P. & Zhang, D. Smart anticorrosion coating based on stimuli-responsive micro/nanocontainer: a review. *J. Oceanol. Limnol.* **38**, 1045–1063 (2020).
28. Li, Z. X. et al. Synergistic effect of hydrophobic film and porous MAO membrane containing alkynol inhibitor for enhanced corrosion resistance of magnesium alloy. *Surf. Coat. Technol.* **357**, 515–525 (2019).
29. Huang, Y. et al. Enhanced corrosion resistance and self-healing effect of sol-gel coating incorporating one-pot-synthesized corrosion inhibitor-encapsulated silica nanocontainers. *J. Sol.-Gel Sci. Technol.* **104**, 78–90 (2022).
30. Li, D. D. et al. Corrosion protection coatings embedded with silane-functionalized rGO/SiO₂ nanocontainers: Enhancing dispersive and corrosion-inhibitor loading capabilities. *Surf. Coat. Technol.* **427**, 127850 (2021).
31. Xing, X. T., Wang, J. H., Li, Q. S. & Hu, W. B. Influence of acid treatment on the loading and release behavior of halloysite with 2-Mercaptobenzothiazole. *J. Nanosci. Nanotechnol.* **19**, 7178–7184 (2019).
32. Xing, X. T. et al. A novel method to control the release rate of halloysite encapsulated Na₂MoO₄ with Ca²⁺ and corrosion resistance for Q235 steel. *Appl. Clay Sci.* **188**, 105492 (2020).
33. Fang, S. et al. Preparation of gallic acid intercalated layered double hydroxide for enhanced corrosion protection of epoxy coatings. *Coatings* **13**, 128 (2023).
34. Xu, T., Zhao, Y., Zhou, J. H. & Hu, J. M. Composite nanocontainers synthesized by in-situ growth of metal organic frameworks on layered double hydroxides having both passive and active protecting capabilities. *Prog. Org. Coat.* **164**, 106695 (2022).
35. Guo, C. B., Lian, Y. B., Huang, C. & Chen, Z. Y. Sustained-release system based on BTA@MOF-5 for self-healing coating application. *Colloids Surf. A.* **654**, 130139 (2022).
36. Zhao, Y., Xu, T., Zhou, J. H. & Hu, J. M. Superhydrophobic nanocontainers for passive and active corrosion protection. *Chem. Eng. J.* **433**, 134039 (2022).
37. Alibakhshi, E., Ghasemi, E., Mahdavian, M., Ramezanzadeh, B. & Yasaei, M. The effect of interlayer spacing on the inhibitor release capability of layered double hydroxide based nanocontainers. *J. Clean. Prod.* **251**, 119676 (2020).
38. Poznyak, S. K. et al. Novel inorganic host layered double hydroxides intercalated with guest organic inhibitors for anticorrosion applications. *ACS Appl. Mater. Inter.* **1**, 2353–2362 (2009).
39. Stimpfling, T., Leroux, F. & Hintze-Bruening, H. Organo-modified layered double hydroxide in coating formulation to protect AA2024 from corrosion. *Colloids Surf. A* **458**, 147–154 (2014).
40. El-Reesh, G. Y. A., Farghali, A. A., Taha, M. & Mahmoud, R. K. Novel synthesis of Ni/Fe layered double hydroxides using urea and glycerol and their enhanced adsorption behavior for Cr(VI) removal. *Sci. Rep.* **10**, 587 (2020).
41. Wang, Y. & Zhang, D. Synthesis, characterization, and controlled release anticorrosion behavior of benzoate intercalated Zn-Al layered double hydroxides. *Mater. Res. Bull.* **46**, 1963–1968 (2011).
42. Du, P., Wang, J., Liu, G. Z., Zhao, H. C. & Wang, L. P. Facile synthesis of intelligent nanocomposites as encapsulation for materials protection. *Mater. Chem. Front.* **3**, 321–330 (2019).
43. Nguyen, T. D. et al. Molybdate intercalated hydrotalcite/graphene oxide composite as corrosion inhibitor for carbon steel. *Surf. Coat. Technol.* **399**, 126165 (2020).
44. Cai, M. et al. In situ assemble Ti₃C₂T_x MXene@MgAl-LDH heterostructure towards anticorrosion and antiwear application. *Chem. Eng. J.* **419**, 130050 (2021).
45. Li, C. H. et al. Cataphoretic deposition of an epoxy coating with the incorporation of Ti₃C₂T_x@Mg-Al layered double hydroxide for long-term active corrosion protection effect. *Prog. Org. Coat.* **175**, 107333 (2023).
46. Wang, H. D. et al. Superlubricity of polyalkylene glycol aqueous solutions enabled by ultrathin layered double hydroxide nanosheets. *ACS Appl. Mater. Inter.* **11**, 20249–20256 (2019).
47. Hou, D. D. et al. Facile synthesis of graphene via reduction of graphene oxide by artemisinin in ethanol. *J. Materomics* **4**, 256–265 (2018).
48. Bouali, A. C. et al. Layered double hydroxides (LDHs) as functional materials for the corrosion protection of aluminum alloys: a review. *Appl. Mater. Today* **21**, 100857 (2020).
49. Fang, L., He, Q. Q., Zhou, M. J., Zhao, J. P. & Hu, J. M. Electrochemically assisted deposition of sol-gel films on graphene nanosheets. *Electrochem. Commun.* **109**, 106609 (2019).
50. Xu, T., Fang, L., Zhao, J. P., Zhang, J. T. & Hu, J. M. A novel graphene/silica composite nanocontainer prepared by electrochemically assisted deposition. *Prog. Org. Coat.* **178**, 107464 (2023).
51. Su, Y. et al. Impermeable barrier films and protective coatings based on reduced graphene oxide. *Nat. Commun.* **5**, 4843 (2014).
52. Topsakal, M., Sahin, H. & Ciraci, S. Graphene coatings: an efficient protection from oxidation. *Phys. Rev. B* **85**, 155445 (2012).
53. Li, Z. H. et al. Fast electrosynthesis of Fe-containing layered double hydroxide arrays toward highly efficient electrocatalytic oxidation reactions. *Chem. Sci.* **6**, 6624–6631 (2015).
54. Li, C. G., Bao, Y. P., Liu, E. Z., Zhao, B. R. & Sun, T. Recent advances of modified Ni (Co, Fe)-based LDH 2D materials for water splitting. *Molecules* **28**, 1475 (2023).
55. Vlamidis, Y., Scavetta, E., Giorgetti, M., Sangiorgi, N. & Tonelli, D. Electrochemically synthesized cobalt redox active layered double hydroxides for supercapacitors development. *Appl. Clay Sci.* **143**, 151–158 (2017).
56. Bai, J. F., Liu, Y., Yin, X. H., Duan, H. T. & Ma, J. H. Efficient removal of nitrobenzene by Fenton-like process with Co-Fe layered double hydroxide. *Appl. Surf. Sci.* **416**, 45–50 (2017).
57. Zhang, J. P., Xia, Q., Hong, X. F., Chen, J. J. & Liu, D. J. Synthesis of layered double hydroxides with nitrate and its adsorption properties of phosphate. *Water Sci. Technol.* **83**, 100–110 (2021).
58. Carneiro, J. et al. Polyelectrolyte-modified layered double hydroxide nanocontainers as vehicles for combined inhibitors. *RSC Adv.* **5**, 39916–39929 (2015).
59. Serdechnova, M. et al. Interlayer intercalation and arrangement of 2-mercaptobenzothiazolate and 1,2,3-benzotriazololate anions in layered double hydroxides: In situ X-ray diffraction study. *J. Solid State Chem.* **233**, 158–165 (2016).
60. Remyamol, T., John, H. & Gopinath, P. Synthesis and nonlinear optical properties of reduced graphene oxide covalently functionalized with polyaniline. *Carbon* **59**, 308–314 (2013).
61. Stimpfling, T. et al. Amino acid interleaved layered double hydroxides as promising hybrid materials for AA2024 corrosion inhibition. *Eur. J. Inorg. Chem.* 2006–2016 (2016).
62. Yang, L. N. et al. In situ NH₂-functionalized graphene oxide/SiO₂ composites to improve Cu(II) removal from ammoniacal solutions. *Chem. Eng. J.* **306**, 77–85 (2016).
63. Bujdosó, T., Patzkó, A., Galbács, Z. & Dékány, I. Structural characterization of arsenate ion exchanged MgAl-layered double hydroxide. *Appl. Clay Sci.* **44**, 75–82 (2009).
64. Maia, F. et al. Corrosion protection of AA2024 by sol-gel coatings modified with MBT-loaded polyurea microcapsules. *Chem. Eng. J.* **283**, 1108–1117 (2016).
65. Chen, X. N., Wang, X. H. & Fang, D. A review on C1s XPS-spectra for some kinds of carbon materials. *Fuller. Nanotub. Car. N.* **28**, 1048–1058 (2020).
66. Vesel, A., Zaplotnik, R., Primc, G. & Mozetic, M. A Review of Strategies for the Synthesis of N-Doped Graphene-Like Materials. *Nanomaterials-Basel* **10**, 2286 (2020).
67. Ma, K. Y. et al. Dependence of Co/Fe ratios in Co-Fe layered double hydroxides on the structure and capacitive properties. *Electrochim. Acta* **198**, 231–240 (2016).

68. Xie, W. J., Weng, L. T., Ng, K. M., Chan, C. K. & Chan, C. M. Defects of clean graphene and sputtered graphite surfaces characterized by time-of-flight secondary ion mass spectrometry and X-ray photoelectron spectroscopy. *Carbon* **112**, 192–200 (2017).
69. Xie, W. J., Weng, L. T., Yeung, K. L. & Chan, C. M. Repair of defects created by Ar⁺ sputtering on graphite surface by annealing as confirmed using ToF-SIMS and XPS. *Surf. Interface Anal.* **50**, 851–859 (2018).
70. Tedim, J. et al. Zn-Al layered double hydroxides as chloride nanotraps in active protective coatings. *Corros. Sci.* **55**, 1–4 (2012).
71. Hirschorn, B. et al. Determination of effective capacitance and film thickness from constant-phase-element parameters. *Electrochim. Acta* **55**, 6218–6227 (2010).
72. Miskovic-Stankovic, V. B., Stanic, M. R. & Drazic, D. M. Corrosion protection of aluminium by a cataphoretic epoxy coating. *Prog. Org. Coat.* **36**, 53–63 (1999).
73. Brug, G. J., Vandeneeden, A. L. G., Sluytersrehabach, M. & Sluyters, J. H. The analysis of electrode impedances complicated by the presence of a constant phase element. *J. Electroanal. Chem.* **176**, 275–295 (1984).
74. Li, D. O. et al. Covalent chemical functionalization of semiconducting layered chalcogenide nanosheets. *Mol. Syst. Des. Eng.* **4**, 962–973 (2019).
75. Shi, Z. Y., Ge, Y. Y., Yun, Q. B. & Zhang, H. Two-dimensional nanomaterial-templated composites. *Acc. Chem. Res.* **55**, 3581–3593 (2022).
76. de Luna, M. S. et al. Long-lasting efficacy of coatings for bronze artwork conservation: the key role of layered double hydroxide nanocarriers in protecting corrosion inhibitors from photodegradation. *Angew. Chem. Int. Ed.* **57**, 7380–7384 (2018).

Acknowledgements

This work was supported by the National Natural Science Foundation of China (No. 52071283), the Zhejiang Provincial Natural Science Foundation of China, and the Zhejiang Province High-level Talent Supporting Program (2022R52001).

Author contributions

Teng Xu: Investigation, Data curation, Writing- original draft. Qian-Yu Wang: Investigation. Jin-Tao Zhang: Data Curation. Ji-Ming Hu: Conceptualization, Funding acquisition, Writing- Reviewing & Editing.

Competing interests

The authors declare no competing interests.

Additional information

Supplementary information The online version contains supplementary material available at <https://doi.org/10.1038/s41529-024-00443-z>.

Correspondence and requests for materials should be addressed to Ji-Ming Hu.

Reprints and permissions information is available at <http://www.nature.com/reprints>

Publisher's note Springer Nature remains neutral with regard to jurisdictional claims in published maps and institutional affiliations.

Open Access This article is licensed under a Creative Commons Attribution 4.0 International License, which permits use, sharing, adaptation, distribution and reproduction in any medium or format, as long as you give appropriate credit to the original author(s) and the source, provide a link to the Creative Commons licence, and indicate if changes were made. The images or other third party material in this article are included in the article's Creative Commons licence, unless indicated otherwise in a credit line to the material. If material is not included in the article's Creative Commons licence and your intended use is not permitted by statutory regulation or exceeds the permitted use, you will need to obtain permission directly from the copyright holder. To view a copy of this licence, visit <http://creativecommons.org/licenses/by/4.0/>.

© The Author(s) 2024